

Toward cubic symmetry for Ir^{4+} : structure and magnetism of the antiferroite K_2IrBr_6

Nazir Khan,^{1,*} Danil Prishchenko,² Mary H. Upton,³ Vladimir G. Mazurenko,² and Alexander A. Tsirlin^{1,2,†}

¹*Experimental Physics VI, Center for Electronic Correlations and Magnetism,
Institute of Physics, University of Augsburg, 86135 Augsburg, Germany*

²*Ural Federal University, Mira Str. 19, 620002 Ekaterinburg, Russia*

³*Advanced Photon Source, Argonne National Laboratory, Argonne, Illinois 60439, USA*

Crystal structure, electronic state of Ir^{4+} , and magnetic properties of the antiferroite compound K_2IrBr_6 are studied using high-resolution synchrotron x-ray diffraction, resonant inelastic x-ray scattering (RIXS), thermodynamic and transport measurements, and *ab initio* calculations. The crystal symmetry is reduced from cubic at room temperature to tetragonal below 170 K and eventually to monoclinic below 122 K. These changes are tracked by the evolution of the non-cubic crystal-field splitting Δ measured by RIXS. Non-monotonic changes in Δ are ascribed to the competing effects of the tilt, rotation, and deformation of the IrBr_6 octahedra as well as tetragonal strain on the electronic levels of Ir^{4+} . The Néel temperature of $T_N = 11.9$ K exceeds that of the isostructural K_2IrCl_6 , and the magnitude of frustration on the fcc spin lattice decreases. We argue that the replacement of Cl by Br weakens electronic correlations and enhances magnetic couplings.

I. INTRODUCTION

Spin-orbit coupling can have major effect on the electronic structure and magnetism of $5d$ transition metals [1, 2]. The extent of spin-orbit physics depends on whether the orbital moment of a $5d$ ion is fully or partially quenched – an effect that hinges upon details of crystal-field levels and local environment of the transition-metal atom. For example, electronic state of the $5d^5$ Ir^{4+} ion can change from mundane spin- $\frac{3}{2}$ in square-planar IrO_4 complexes [3, 4] to a more exotic $j_{\text{eff}} = \frac{1}{2}$ in the regular IrO_6 octahedral environment, which has interesting implications for spin-liquid physics and unusual metallic states [5–7].

Experimental studies of iridates suggest that even minor deviations from the ideal symmetry of an IrO_6 octahedron may cause appreciable non-cubic crystal-field splittings Δ . Many of the compounds studied to date – including honeycomb iridates [8], double perovskites [9, 10], and fluorides [11] – show the nearly constant Δ of about 150 meV [12]. This similarity goes across different structure types, with the Δ value being remarkably insensitive to the structural motif or crystallographic symmetry. For example, similar values of Δ were reported for monoclinic $\text{Sr}_2\text{CeIrO}_6$ and nominally cubic $\text{Ba}_2\text{CeIrO}_6$ [9, 10]. This raises a natural question of which structural parameters determine Δ in the limit of weak local distortions, and whether Δ values below 150 meV can be reached in a real Ir^{4+} material.

Here, we shed light on this problem by studying K_2IrBr_6 and report $\Delta \simeq 50$ meV, the lowest value of a non-cubic crystal-field splitting achieved so far in an Ir^{4+} compound. We also track the influence of different structural distortions on this parameter by monitoring Δ upon cooling whilst the compound progressively reduces

its symmetry via two consecutive structural phase transitions. K_2IrBr_6 belongs to the family of Ir^{4+} antiferroites, material realizations of frustrated spin- $\frac{1}{2}$ fcc antiferromagnets [13–15], and we also investigate how symmetry lowering changes the strength of electronic correlations and magnetic couplings as well as the magnitude of magnetic frustration in this family of compounds. Our results are complementary to the very recent study of the Ir^{4+} antiferroites [16] where similarly low values of Δ were reported for K_2IrBr_6 , K_2IrCl_6 , and other compounds of the same family, but temperature evolution of Δ and its interplay with the structural parameters were not explored.

The manuscript is organized as follows. Sec. II contains methodological details. In Sec. III, we report crystal structure of K_2IrBr_6 as a function of temperature, analyze individual distortions, and discuss phonon instabilities that lead to consecutive structural phase transitions in this compound. Sec. IV describes the electronic state of Ir^{4+} studied by resonant inelastic x-ray scattering and *ab initio* calculations across the different polymorphs. Sec. V contains the results of thermodynamic measurements and *ab initio* calculations of exchange couplings that both probe low-temperature magnetism of K_2IrBr_6 . Sec. VI concludes the manuscript with a brief discussion and summary.

II. METHODS

K_2IrBr_6 powder was obtained from ChemPUR GmbH and Alfa Aesar (Ir 25.4% min). Its phase purity was confirmed by room-temperatures powder x-ray diffraction (XRD) data collected at the Rigaku MiniFlex diffractometer ($\text{Cu } K_\alpha$ radiation). Single crystals were grown from the solution prepared using this powder. A nearly saturated and slightly acidic ($\text{pH} \sim 2$) aqueous solution of K_2IrBr_6 was placed into a glass beaker and kept inside a box furnace with temperature maintained at 60°C , for the nucleation of the crystals by slow evaporation of wa-

* nazirkhan91@gmail.com

† altsirlin@gmail.com

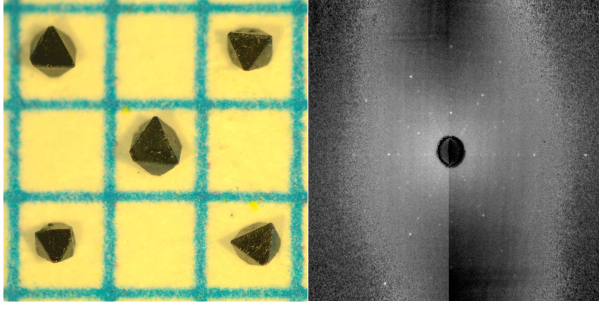


FIG. 1. Image of selected crystals on a mm graph paper and x-ray Laue diffraction pattern of a K_2IrBr_6 single crystal.

ter from the solution. After 4 days many small crystals with the typical size of about $(0.7 \times 0.6 \times 0.4) \text{ mm}^3$ were found at the bottom of the glass beaker (Fig. 1). X-ray Laue diffraction experiment confirmed high crystallinity of these samples. The back scattered Laue diffraction pattern with x-ray beam parallel to the normal of the crystal face exhibits three-fold symmetry of the reciprocal space (Fig. 1), and thereby confirms that all naturally occurring crystal faces belong to the family of $\{111\}_c$ crystallographic planes, where the subscript indicates plane indices given with respect to the cubic axes of the room-temperature K_2IrBr_6 structure.

Temperature-dependent crystallographic study was performed on powder, because high resolution was required, and extensive twinning of the crystal could be expected upon symmetry lowering. High-resolution powder XRD was performed at the ID22 beamline of the European Synchrotron Radiation Facility (Grenoble, France) using the wavelength $\lambda = 0.40001 \text{ \AA}$ at temperatures down to 20 K stabilized using He flow cryostat. Structure refinement was performed using the JANA2006 software [17]. Additionally, structural phase transitions were probed by a thermal expansion measurement down to 1.78 K using a highly sensitive capacitive dilatometer [18] operated within Quantum Design PPMS. The data were collected in both heating and cooling cycles with a temperature sweep rate of 0.2 K/min.

Resonant inelastic x-ray scattering (RIXS) measurements were performed on the single crystal of K_2IrBr_6 using the MERIX spectrometer on beamline 27-ID of the Advance Photon Source (APS) at Argonne National Laboratory to investigate crystal-field excitations of Ir^{4+} . The incident x-ray energy was tuned to the Ir L_3 absorption edge at 11.215 keV.

Temperature and field dependence of the dc magnetization was measured on powder, on individual single crystals, and on a stack of co-aligned single crystals with the total mass of 2.8 mg using the Quantum Design SQUID-VSM magnetometer (MPMS 3). Pulsed-field magnetization data up to 57 T were collected in the Dresden High Magnetic Field Laboratory on the powder sample [19]. The pulsed-field data were then scaled with the magnetization data measured with the SQUID-VSM

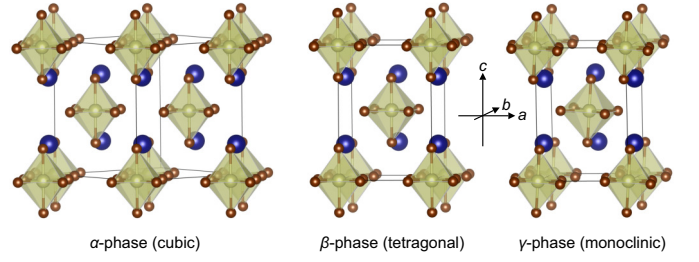


FIG. 2. Crystal structures of the K_2IrBr_6 polymorphs.

magnetometer in static fields up to 7 T.

Specific heat of the K_2IrBr_6 single crystal was measured down to 0.5 K using Quantum Design Physical Properties Measurement System (QD-PPMS) equipped with ^3He refrigerator. The conventional two- τ relaxation method was used.

The temperature dependence of the dc electrical resistivity was measured using B2987A Electrometer/High Resistance Meter in a commercial PPMS cryostat equipped with a home-made resistivity set-up. Standard two-probe method was employed for the resistivity measurement where two Cu wires were attached to the sample with high-conducting silver paste. The electric field was along the $\langle 111 \rangle_c$.

Orbital energies and exchange couplings were assessed by scalar-relativistic density-functional (DFT) band-structure calculations performed in the FPL0 code [20] using the $8 \times 8 \times 6$ k-mesh for the tetragonal and monoclinic structures. Phonon spectra were calculated in PHONOPY via the frozen-phonon method [21]. The forces for the phonon calculations were obtained from DFT and DFT+ U +SO calculations in VASP [22, 23] using the $2 \times 2 \times 1$ supercell and 0.01 \AA atomic displacements. Perdew-Burke-Ernzerhof flavor of the exchange-correlation potential [24] was chosen for all calculations. DFT+ U +SO calculations utilized double-counting correction in the atomic limit and the Hund's coupling parameter $J = 0.3 \text{ eV}$. The choice of the on-site Coulomb repulsion parameter U is further discussed in Sec. IV B.

III. STRUCTURAL TRANSFORMATIONS

Antifluorite-type crystal structure of K_2IrBr_6 features isolated IrBr_6 octahedra arranged on the sites on an fcc lattice and separated by K atoms (Fig. 2). The idealized structure is cubic, but rotations, tilts, and deformations of the octahedra may lead to different types of symmetry lowering.

Early temperature-dependent studies reported two phase transitions in K_2IrBr_6 at 182 K and 13 K from differential thermal analysis and calorimetry [25]. No diffraction experiments were performed. Our thermal expansion (Fig. 3) and specific heat (Fig. 13) data confirm the transitions around 170 K and 12 K, respectively. Magnetic susceptibility changes upon the latter transi-

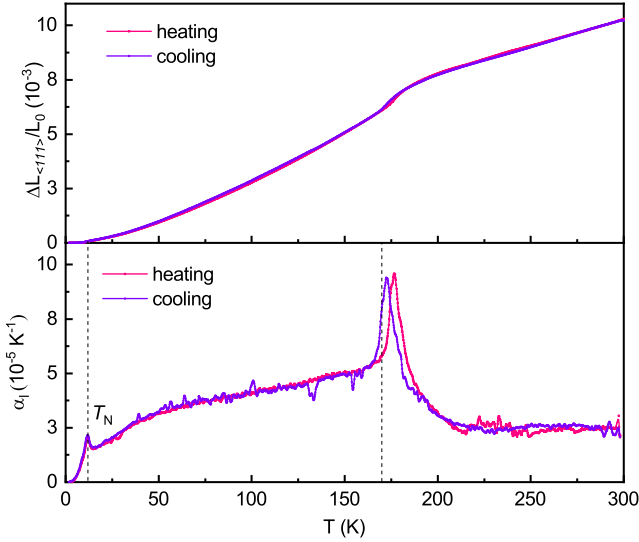


FIG. 3. Relative length change $\Delta L/L$ of the K_2IrBr_6 single crystal measured along the $\langle 111 \rangle_c$ crystallographic direction, and the corresponding linear thermal expansion coefficient, $\alpha_l = 1/L_0[d(\Delta L)/dT]$, as a function of temperature. Hysteretic behavior is clearly seen at the α – β transition around 170 K. A weaker anomaly around 12 K indicates the onset of magnetic long-range order.

tion (Fig. 12) suggesting magnetic ordering rather than structural transformation as the primary origin of this anomaly. High-resolution XRD additionally shows another structural phase transition around 120 K that lacks any signatures in thermodynamic measurements. Cubic symmetry of the room-temperature crystal structure (α - K_2IrBr_6) is reduced to tetragonal below 170 K (β - K_2IrBr_6) and to monoclinic below 122 K (γ - K_2IrBr_6). This sequence of structural phase transitions is consistent with the very recent neutron diffraction study [16].

A. Cubic α -phase

At 270 K, sharp and non-split reflections measured by high-resolution synchrotron XRD (Fig. 4) confirm cubic symmetry of the crystal structure. The refined lattice parameter $a = 10.29266(2) \text{ \AA}$ is consistent with the reported room-temperature value of $a = 10.298(5) \text{ \AA}$ [26]. Br atoms are at $(x, 0, 0)$ with the Ir–Br distance of $2.466(2) \text{ \AA}$, about 0.15 \AA longer than in isostructural K_2IrCl_6 [14].

The inspection of atomic displacement parameters (ADPs) at 270 K revealed anomalously high values for K and Br (Table I). In the case of Br, displacement ellipsoid is stretched in the direction perpendicular to the Ir–Br bond ($U_{22} = U_{33} \gg U_{11}$) and indicates disordered rotations of the IrBr_6 octahedra. Similar features have been reported in isostructural K_2IrCl_6 [14].

The rotation angle φ is gauged using the transverse component of the Br ADP. With $U_{22} = U_{33} = \langle (\Delta r)^2 \rangle$,

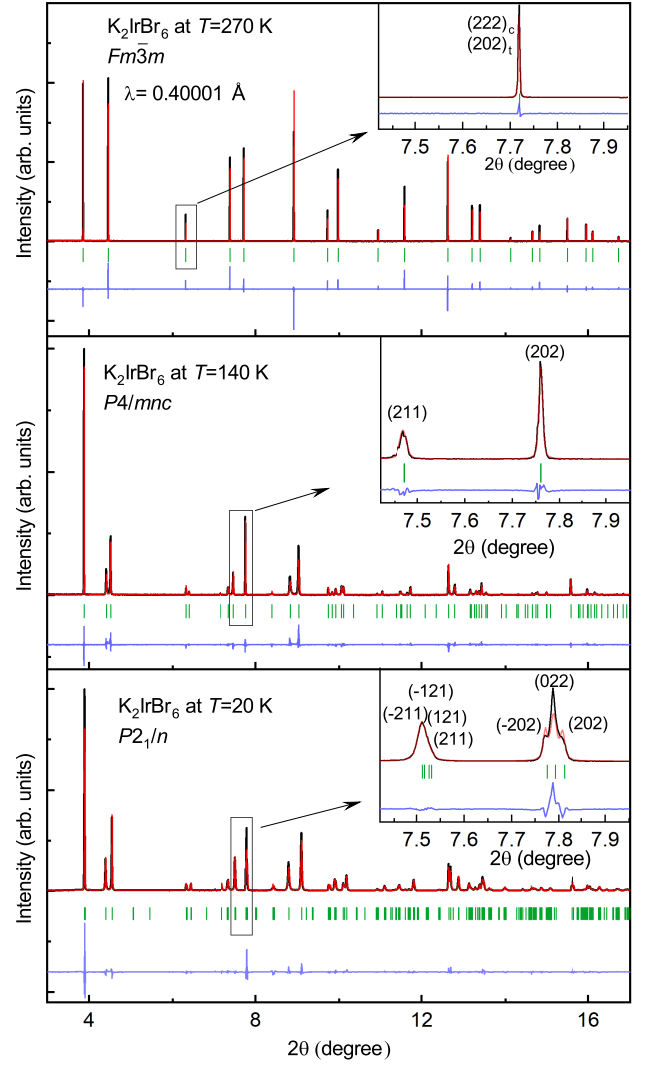


FIG. 4. Structure refinements for α - K_2IrBr_6 at 270 K, β - K_2IrBr_6 at 140 K, and γ - K_2IrBr_6 at 20 K. The solid red lines are the calculated patterns. The insets show the temperature evolution of the cubic (222) reflection, which at 20 K exhibits a clear monoclinic splitting, whereas the (211) reflection is forbidden in the fcc structure and appears only in the β -phase.

one estimates $\varphi = \tan^{-1}(\sqrt{U_{22}}/d)$, where d is the Ir–Br distance. Temperature evolution of φ (Fig. 5) reveals that the rotations are gradually suppressed upon cooling, but remain sizable even at 170 K where they condense causing the α – β transition.

B. Tetragonal β -phase

Below 170 K, additional reflections incompatible with the face-centered cubic structure appeared in the XRD pattern (Fig. 4). They could be indexed in a primitive tetragonal unit cell with $a_{\text{tet}} = a_{\text{cub}}/\sqrt{2}$ and $c_{\text{tet}} = c_{\text{cub}}$. The crystal structure was refined in the space group $P4/mnc$ determined previously for Rb_2TeI_6 [27] and sev-

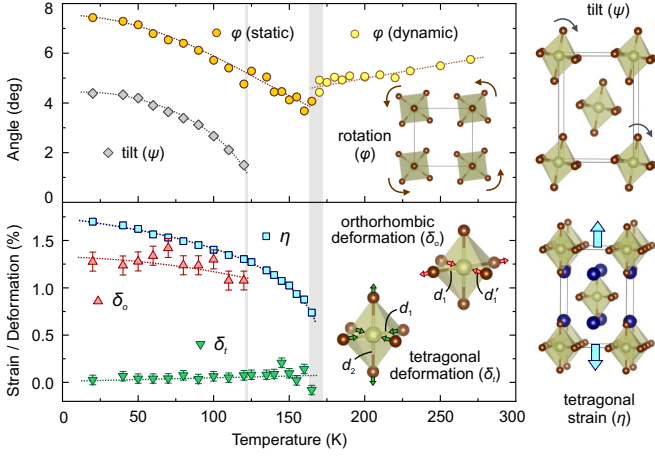


FIG. 5. Distortions of the K_2IrBr_6 structure. Upper panel: rotation (φ) and tilt (ψ) of the IrBr_6 octahedra. Lower panel: tetragonal (δ_t) and orthorhombic (δ_o) deformations of the octahedra, as well as tetragonal strain (η). See text for the definitions of δ_t , δ_o , and η . The lines are guide for the eye.

eral other distorted antiferro compounds [28, 29]. K and Ir positions remain fully constrained by symmetry, whereas the Br position splits into two, resulting in two types of distortions: i) cooperative rotations of the IrBr_6 octahedra in the ab plane; ii) tetragonal deformation of the octahedra. Our structure refinement shows that the distortion is dominated by the former effect. The rotation angle φ lies in the range of $4 - 5^\circ$ (Fig. 5) suggesting that dynamic rotations in the α -phase become static below the transition. Tetragonal deformation is gauged by $\delta_t = (d_2 - d_1)/(d_1 + d_2)$, where d_1 and d_2 are the in-plane and out-of-plane distances in the IrBr_6 octahedron, respectively. This deformation remains negligible throughout the stability range of the β -phase.

First-order nature of the $\alpha - \beta$ transition can be inferred from the hysteretic behavior seen in the thermal expansion measurement (Fig. 3) and from phase coexistence revealed by XRD. At several temperatures around the transition (Fig. 6), both cubic and tetragonal phases were present in the sample, with the fraction of the β -phase decreasing from 76 % at 165 K to 26 % at 170 K upon heating [30].

The cubic-to-tetragonal transition in antiferro compounds is caused by soft phonon modes observed at the zone center (Γ) and zone boundary (X) [31, 32]. Indeed, our phonon calculations for $\alpha\text{-K}_2\text{IrBr}_6$ reveal an imaginary phonon band along $\Gamma - X$ (Fig. 7). This instability present in both DFT and DFT+ U +SO calculations is a rotary mode that causes dynamic rotations of the IrBr_6 octahedra. It originates from a size mismatch between the octahedra and K atoms [33].

The condensation of a soft phonon mode normally leads to a second-order phase transition, as reported in K_2OsCl_6 [34, 35], K_2ReCl_6 [36], and K_2TeBr_6 [29]. In contrast, our data reveal strong signatures of a first-order transition, even though it follows group-subgroup rela-

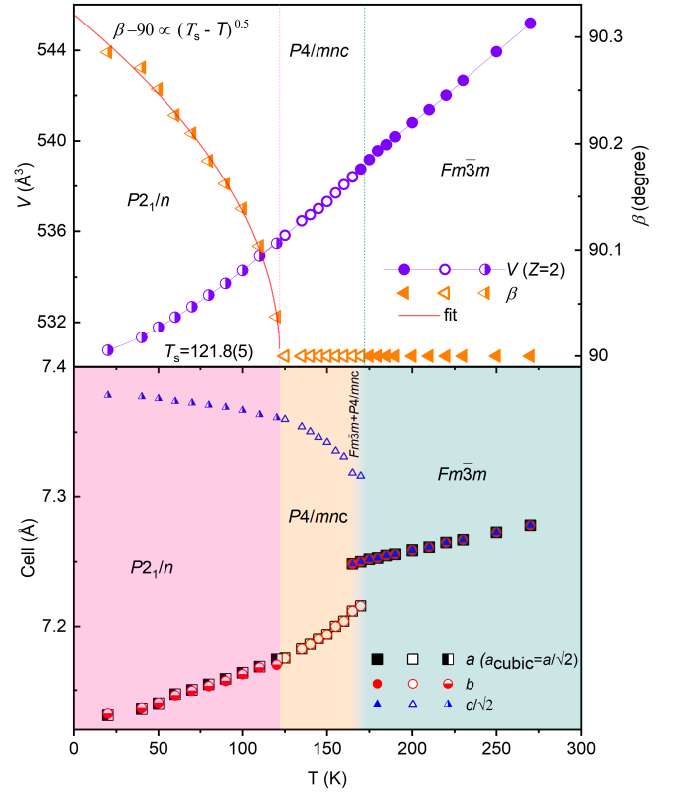


FIG. 6. Lattice parameters of K_2IrBr_6 . Upper panel: unit cell volume (two formula units) and monoclinic angle β along with the power-law fit described in the text. Lower panel: a , b , and $c/\sqrt{2}$ given in the setting of β - and γ - K_2IrBr_6 .

tion, and octahedral rotations serve as the primary order parameter. In K_2IrBr_6 , first-order character of the transition is likely caused by a strong coupling to the tetragonal strain [37], $\eta = (a_{\text{tetr}} - c_{\text{tetr}}/\sqrt{2})/(a_{\text{tetr}} + c_{\text{tetr}}/\sqrt{2})$, that appears abruptly at the transition ($\eta_{170\text{K}} = 0.69\%$) and systematically increases down to low temperatures ($\eta_{20\text{K}} = 1.72\%$), as shown in Fig. 5. In contrast, K_2TeBr_6 with the second-order $\alpha - \beta$ transition features $\eta \simeq 0$ at the transition, followed by a linear increase of η to 0.39% within a narrow temperature range below the transition, and an eventual decrease down to $\eta = 0.33\%$ at 20 K [29].

C. Monoclinic γ -phase

The second structural phase transition in K_2IrBr_6 has no fingerprints in thermal expansion or specific heat, but can be clearly seen in high-resolution XRD data where (202) reflection of the β -phase splits into three peaks indicative of a monoclinic distortion (Fig. 4). The absence of this splitting above 120 K attests tetragonal symmetry of the β -phase and suggests that an additional phase transition should take place at the temperature where peak splitting appears. This transition is further evidenced by the RIXS data that probe local environment of

TABLE I. Structural parameters of α -K₂IrBr₆ at 270 K, β -K₂IrBr₆ at 140 K, and γ -K₂IrBr₆ at 20 K. The error bars are from the Rietveld refinement. Atomic displacement parameters U_{iso} are given in Å². All the crystallographic sites are fully occupied. The R_I and R_p are refinement residuals for the peak intensities and peak profile, respectively [30].

| $T(K)$ | 270 K | 140 K | 20 K |
|-----------------|--|--|--|
| Space group | $Fm\bar{3}m$ | $P4/mnc$ | $P2_1/n$ |
| $a(\text{\AA})$ | 10.29266(2) | 7.18558(8) | 7.13121(10) |
| $b(\text{\AA})$ | 10.29266(2) | 7.18558(8) | 7.13240(10) |
| $c(\text{\AA})$ | 10.29266(2) | 10.39521(14) | 10.43467(15) |
| β (deg) | 90 | 90 | 90.2857(5) |
| R_I/R_p | 0.0765/0.1663 | 0.0699/0.1720 | 0.0303/0.0923 |
| Ir | $4a$ (0,0,0) $U_{\text{iso}} = 0.0166(1)$ | $2a$ (0,0,0) $U_{\text{iso}} = 0.0115(4)$ | $2a$ (0,0,0) $U_{\text{iso}} = 0.0033(4)$ |
| K | $8c$ ($\frac{1}{4}, \frac{1}{4}, \frac{1}{4}$) $U_{\text{iso}} = 0.0409(6)$ | $4d$ ($0, \frac{1}{2}, \frac{1}{4}$) $U_{\text{iso}} = 0.0317(15)$ | $4e$ (x, y, z) $x = -0.0077(8)$ $y = 0.4941(14)$ $z = 0.2583(6)$ $U_{\text{iso}} = 0.0143(16)$ |
| Br(1) | $24e$ ($x, 0, 0$) $x = 0.2373(1)$ $U_{\text{iso}} = 0.0346(4)$ | $4e$ (0,0, z) $z = 0.2376(2)$ $U_{\text{iso}} = 0.0295(4)$ | $4e$ (x, y, z) $x = 0.0263(3)$ $y = -0.0030(7)$ $z = 0.2361(1)$ $U_{\text{iso}} = 0.0087(7)$ |
| Br(2) | | $8h$ ($x, y, 0$) $x = 0.2231(2)$ $y = 0.2607(2)$ $U_{\text{iso}} = 0.0295(4)$ | $4e$ (x, y, z) $x = 0.2803(4)$ $y = -0.2106(3)$ $z = -0.0125(2)$ $U_{\text{iso}} = 0.0136(6)$ |
| Br(3) | | | $4e$ (x, y, z) $x = 0.2156(3)$ $y = 0.2638(3)$ $z = -0.0102(2)$ $U_{\text{iso}} = 0.0136(6)$ |

Ir⁴⁺ and its non-cubic crystal-field splitting (see Sec. IV). In the case of K₂PtBr₆, a spectroscopic probe (nuclear quadrupolar resonance) was also shown to be most sensitive to distortions beyond tetragonal symmetry in antiferrofluorite hexahalide compounds [38].

The monoclinic angle increases upon cooling. Its temperature dependence can be approximated by $(\beta - 90^\circ) \propto (T_s - T)^{0.5}$ and returns the transition temperature of $T_s = 121.8(5)$ K. The power-law evolution of β corresponds to a second-order phase transition in agreement with the absence of a volume change or hysteresis around T_s (Fig. 6).

Symmetry lowering toward $P2_1/n$ allows several types of distortions, most notably the tilt of the IrBr₆ octahedra relative to the c -axis and the orthorhombic deformation of the octahedra (Figs. 2 and 5). The $\beta - \gamma$ transition is driven by a phonon instability of the β -phase where imaginary phonon modes are found around the Γ -point (Fig. 7). Although metrically tetragonal, β -phase still features a significant amount of dynamic disorder, as

seen from the increased ADPs of K and Br atoms (Table I). In contrast, the γ -phase shows much lower ADPs. This structure is dynamically stable, with no imaginary phonon frequencies in DFT+ U +SO. Imaginary phonons are still obtained in the DFT calculation, but they are a drawback of neglecting Coulomb correlations and spin-orbit coupling, similar to α -RuCl₃ where the spurious dimerized state is stabilized on the DFT level [39].

Detailed analysis of the γ -phase structure shows that orthorhombic strain (the difference between a and b) remains negligible, whereas tetragonal strain η increases steadily upon cooling (Fig. 5). In-plane octahedral rotations φ increase too and reach nearly 7.5° at 20 K. Additionally, the octahedral tilt ψ and the orthorhombic deformation δ_o develop below the $\beta - \gamma$ transition (Fig. 5). Here, we define $\delta_o = (d_1 - d'_1)/(d_1 + d'_1)$, where d_1 and d'_1 are the in-plane distances in the IrBr₆ octahedron. The orthorhombic deformation reaches about 1.3% at 20 K, whereas tetragonal deformation δ_t remains small. In contrast, crystal structures of Ir⁴⁺ oxides are often domi-

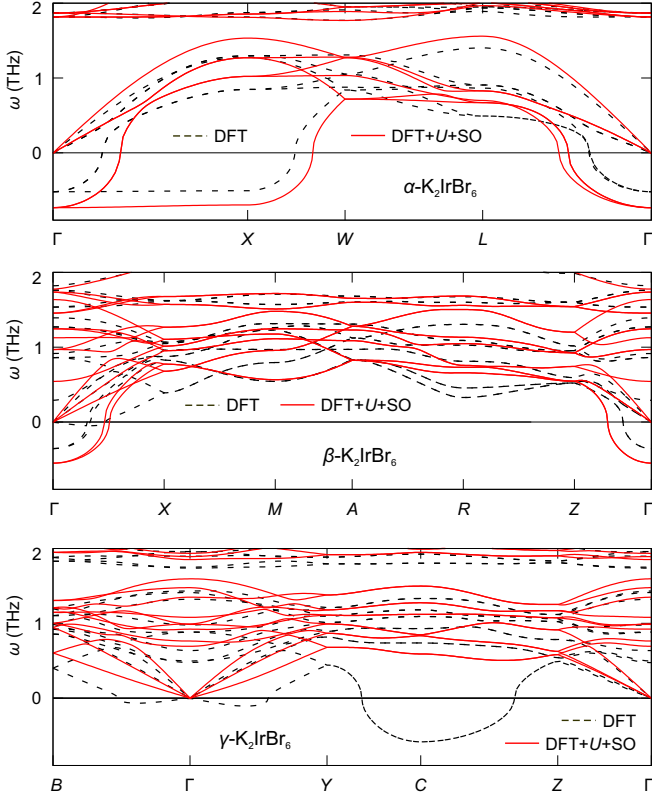


FIG. 7. Calculated phonon spectra for different polymorphs of K_2IrBr_6 . The dashed black and solid red lines are phonon branches obtained within DFT and DFT+U+SO, respectively.

nated by the tetragonal deformation, such as $\delta_t = -1.9\%$ in Sr_2IrO_4 [40] and post-perovskite CaIrO_3 [41].

IV. ELECTRONIC STRUCTURE

A. Crystal-field splitting

Our structural analysis in Sec. III reveals the non-cubic crystal environment of Ir^{4+} in K_2IrBr_6 . Indeed, even in the nominally cubic α -phase rotations of the IrBr_6 octahedra may lower the symmetry locally. To assess the effect of these structural distortions onto the electronic levels of Ir^{4+} , we performed RIXS measurements at the Ir L_3 edge.

Under ideal cubic symmetry and in the presence of spin-orbit coupling, the t_{2g} levels of Ir^{4+} transform into the lower-lying $j_{\text{eff}} = \frac{3}{2}$ and higher-lying $j_{\text{eff}} = \frac{1}{2}$ states. The lowest-energy excitation is then of the $\frac{3}{2} \rightarrow \frac{1}{2}$ nature and appears at $\frac{3}{2}\lambda$, where λ is the spin-orbit coupling constant. K_2IrBr_6 reveals this excitation in the form of a weakly split peak centered around 0.6 eV (Fig. 8). The separation into two peaks manifests residual non-cubic crystal-field splitting in the Ir t_{2g} shell.

For a quantitative analysis, the spectral feature at

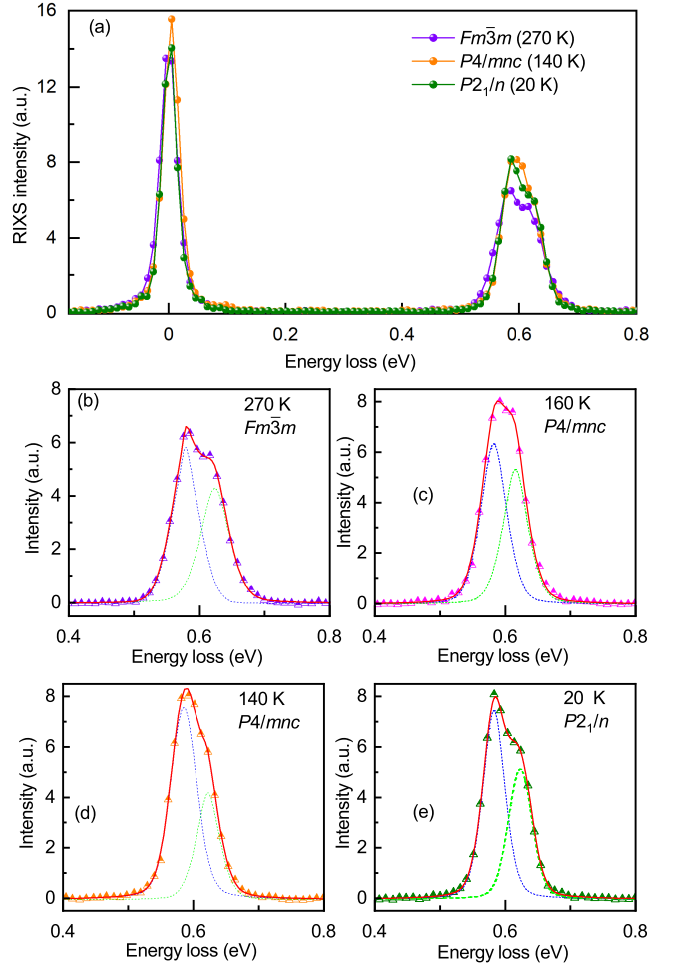


FIG. 8. (a) RIXS spectra measured at the Ir L_3 edge ($E_i = 11.215$ keV) for different polymorphs. The peak at 0 eV corresponds to the strong elastic line, whereas the peaks at 0.5 – 0.7 eV are inelastic lines due to the low-lying excitations. The double-peak structure of this feature manifests a splitting of the $j = \frac{3}{2}$ states. (b-e) Enlarged view of the inelastic lines at selected temperatures. The solid lines are fits with two pseudo-Voigt functions. The fit to the 160 K spectrum in panel (c) returns the lowest crystal-field splitting of $\Delta = 49$ meV.

0.6 eV was fitted to the sum of two pseudo-Voigt functions with the peak positions $\hbar\omega_1$ and $\hbar\omega_2$. Assuming $\Delta \ll \lambda$, one finds $(\hbar\omega_1 + \hbar\omega_2)/2 = \frac{3}{2}\lambda$ and $\Delta = \frac{3}{2}(\hbar\omega_2 - \hbar\omega_1)$ [42] (note the difference to Refs. 9 and 16 where Δ is taken as the separation between $\hbar\omega_1$ and $\hbar\omega_2$ without the $\frac{3}{2}$ pre-factor). We thus estimate $\lambda = 0.40$ eV, which is lower than $\lambda = 0.45 - 0.47$ eV in Ir^{4+} oxides [9, 10] and $\lambda = 0.57$ eV in Ir^{4+} fluorides [11]. This reflects the increased covalency of the Ir–Br interactions, as further discussed in Sec. IV B.

Weak splitting of the t_{2g} levels leads to a slight mixing of the $j_{\text{eff}} = \frac{1}{2}$ and $j_{\text{eff}} = \frac{3}{2}$ states. The ground-state

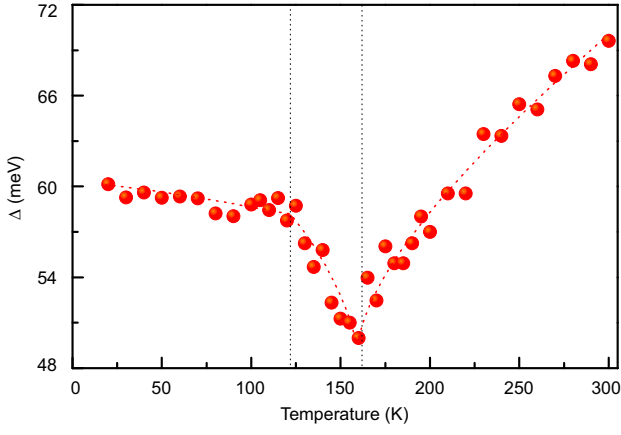


FIG. 9. Temperature dependence of the noncubic crystal-field splitting Δ estimated from the two-peak pseudo-Voigt fits to the RIXS spectra. Dotted lines are guide to the eye.

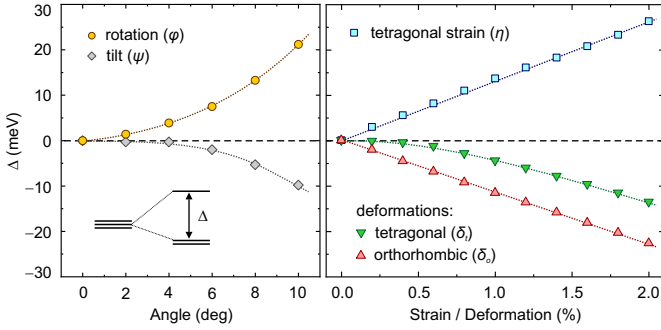


FIG. 10. Noncubic crystal-field splitting Δ calculated for different types of local distortions introduced in Fig. 5. The inset shows the level scheme corresponding to $\Delta > 0$.

wave function of Ir^{4+} in the $|j, j_z\rangle$ basis takes the form

$$|0\rangle = \cos\theta \left| \frac{1}{2}, \frac{1}{2} \right\rangle + \sin\theta \left| \frac{3}{2}, \frac{1}{2} \right\rangle, \quad (1)$$

where the mixing angle θ is given by [2]

$$\tan 2\theta = \frac{4\sqrt{2}\Delta}{2\Delta + 9\lambda}. \quad (2)$$

We estimate $\cos\theta = 0.9993$ using $\Delta \simeq 49$ meV at 160 K. This indicates more than 99.9% contribution of the $j_{\text{eff}} = \frac{1}{2}$ state to the ground-state wavefunction of Ir^{4+} in K_2IrBr_6 . For comparison, this contribution is 99.4% in a typical Ir^{4+} oxide with $\Delta \simeq 150$ meV.

Deviations from the cubic symmetry have a relatively minor influence on the electronic state of Ir^{4+} . Nevertheless, it is instructive to track Δ as a function of temperature and identify main structural effects behind its evolution. Fig. 9 shows that Δ decreases upon cooling within the α -phase, increases in the β -phase, and remains nearly constant in the γ -phase. To elucidate this non-monotonic evolution, we analyzed the effect of individual structural distortions using DFT calculations [30].

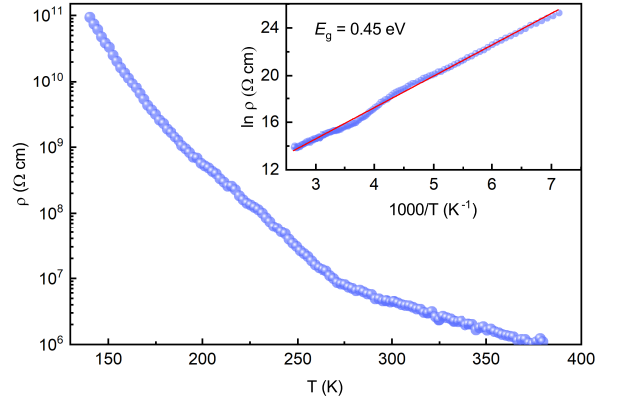


FIG. 11. Temperature dependence of zero-field resistivity (ρ) measured on a single crystal from 380 K down to 140 K with y -axis as log-scale. The resistivity was measured along $\langle 111 \rangle_c$ with electric field $E \parallel \langle 111 \rangle_c$. The inset shows $\ln \rho$ vs $1/T$ and the solid line is the linear fit.

Fig. 10 reveals several trends that may seem counter-intuitive at first glance. Tetragonal strain (η), octahedral rotations (φ), and octahedral tilts (ψ) all cause non-cubic crystal-field splittings, even though no distortion is introduced in the IrBr_6 octahedra. Tetragonal elongation of the octahedra ($\delta_t > 0$) renders $\Delta < 0$, which is opposite to the simple electrostatic picture where elongation stabilizes the d_{yz} and d_{xz} orbitals with $\Delta > 0$. Finally, orthorhombic deformation (δ_o) has a much stronger effect than the tetragonal one [43]. All these observations suggest that atoms beyond nearest-neighbor bromines, and especially K^+ ions that change their positions relative to Br^- , contribute to the non-cubic crystal-field splittings in K_2IrBr_6 . Similar effects of distant neighbors were previously reported in the Ir^{4+} oxides [44].

The non-monotonic temperature evolution of Δ can be understood as follows. In the α -phase, dynamic rotations of the octahedra are gradually suppressed upon cooling. This lowers φ and leads to a monotonic reduction in Δ . The increasing Δ in the β -phase is due to the development of tetragonal strain. On the other hand, the constant Δ value in the γ -phase should be a result of several competing effects, most notably the orthorhombic deformation δ_o that compensates the increased rotations and strain. The lowest $\Delta \simeq 49$ meV is thus reached at the $\alpha - \beta$ transition around 160 – 170 K where octahedral rotations are most strongly suppressed, while tetragonal strain only starts to develop. This puts K_2IrBr_6 in the nearest proximity of the relativistic $j_{\text{eff}} = \frac{1}{2}$ state compared to all materials reported previously. K_2IrCl_6 shows only a slightly larger $\Delta \simeq 72$ meV at 10 K [16].

B. Covalency and correlations

The reduced spin-orbit coupling constant λ gives first indications of the strong hybridization between the Ir and Br states. This hybridization should screen electronic

correlations on the Ir site and thus reduce the band gap. Indeed, our resistivity data reveal a lower band gap compared to isostructural K_2IrCl_6 .

The dc resistivity (ρ) of the K_2IrBr_6 single crystal increases five orders of magnitude upon cooling from 380 K to 140 K and exceeds $4\text{ M}\Omega$ even at room temperature, consistent with the Mott-insulating nature of the compound (Fig. 11). The inset of Fig. 11 shows that the T -dependence of ρ follows the activated behavior

$$\rho(T) = \exp\left(\frac{E_g}{2k_B T}\right), \quad (3)$$

where $E_g \simeq 0.45\text{ eV}$ is the activation energy and k_B is the Boltzmann constant. This activation energy is notably smaller than $E_g \simeq 0.7\text{ eV}$ in K_2IrCl_6 [14].

The effect of electronic correlations is gauged by comparing experimental activation energies E_g with the DFT+ U +SO band gap obtained for different values of U . Best agreement found at $U = 1.8\text{ eV}$ for K_2IrBr_6 and 2.2 eV for K_2IrCl_6 [14] confirms reduced electronic correlations in the bromide compared to the chloride. This result is cross-checked by analyzing ligand contributions to the density of states near the Fermi level in the uncorrelated band structure. We find 51% of Br $4p$ states in K_2IrBr_6 , 43% of Cl $3p$ states in K_2IrCl_6 , and 32% of O $2p$ states in $\text{Ba}_2\text{CeIrO}_6$ as the best oxide analog of antiferrotype hexahalides. This indicates the increase in covalency from oxides to chlorides and bromides of Ir^{4+} . Another experimental signature of strong covalency in iridium halides is the Ir^{4+} magnetic form-factor that shows acute deviations from the ionic value in the case of K_2IrCl_6 [45].

V. LOW-TEMPERATURE MAGNETISM

A. Magnetization

Magnetic response of K_2IrBr_6 is nearly isotropic. In Fig. 12a, we show that magnetic susceptibility data collected on powder and on a stack of co-aligned single crystals are nearly indistinguishable. Individual single crystals had the weight of $0.1 - 0.2\text{ mg}$ and were too small for a high-precision measurement up to room temperature. Nevertheless, with the accuracy feasible for such a small sample no directional dependence of the magnetization could be observed either [30]. This result is consistent with the isotropic nature of nearly $j_{\text{eff}} = \frac{1}{2}$ moments of Ir^{4+} .

Inverse susceptibility measured on single crystals reveals a small step at the $\alpha - \beta$ transition around 170 K (Fig. 12b). We used the temperature range above the transition for a Curie-Weiss fit,

$$\chi(T) = \chi_0 + \frac{N_A \mu_{\text{eff}}^2}{3k_B(T - \Theta_{\text{CW}})}, \quad (4)$$

where $\chi_0 = \chi_{\text{dia}} + \chi_{\text{vV}}$ is the temperature-independent contribution due to core diamagnetism and van Vleck

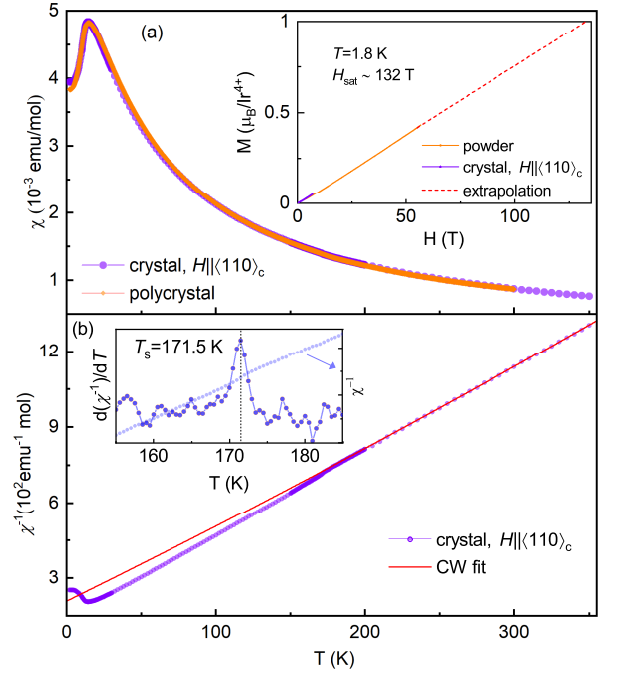


FIG. 12. (a) Temperature dependence of dc-magnetic susceptibility (χ) measured on powder ($\mu_0 H = 0.1\text{ T}$) and on a stack of co-aligned single crystals with the field applied along $\langle 110 \rangle_c$ ($\mu_0 H = 3\text{ T}$). The inset shows field dependence of dc-magnetization measured at 1.8 K in pulsed fields (on powder), and the dotted line is the linear extrapolation to the saturation magnetization of $1 \mu_B$ expected for $j = \frac{1}{2}$ and $g = 2$. (b) T -dependence of the inverse susceptibility χ^{-1} for the single crystal assembly. The solid red line is the Curie-Weiss (CW) fit to the $\chi^{-1}(T)$ data at $215 \leq T \leq 350\text{ K}$. The inset shows the $\chi^{-1}(T)$ and $d(\chi^{-1}(T))/dT$ in the vicinity of the $\alpha - \beta$ structural phase transition.

paramagnetism, N_A is Avogadro's number, k_B is Boltzmann constant, μ_{eff} is paramagnetic effective moment, and Θ_{CW} is the Curie-Weiss temperature. The fitted value of $\chi_0 = -7.08 \times 10^{-5} \text{ emu/mol}$ can be compared to $\chi_{\text{dia}} = -2.66 \times 10^{-4} \text{ emu/mol}$ [46] and yields $\chi_{\text{vV}} = 1.95 \times 10^{-4} \text{ emu/mol}$, which is on par with the van Vleck terms in other Ir^{4+} compounds [14, 47].

The fitted value of paramagnetic effective moment, $\mu_{\text{eff}} = 1.68 \mu_B$, is slightly lower than $1.73 \mu_B$ expected for the $j_{\text{eff}} = \frac{1}{2}$ state with $g = 2$. The fitting is done in the temperature range of the cubic α -phase that features extensive local disorder (Sec. III), but we deem this disorder unlikely to influence μ_{eff} , because similar dynamic disorder has been also reported for K_2IrCl_6 , where the expected value of $\mu_{\text{eff}} = 1.73 \mu_B$ is readily obtained from the Curie-Weiss fitting [14]. Moreover, the electronic state of Ir^{4+} in K_2IrBr_6 remains very close to $j_{\text{eff}} = \frac{1}{2}$ even in the α -phase (Sec. IV). Another possibility is that the temperature range of the fit was not high enough to reach the Curie-Weiss regime. Indeed, $\Theta_{\text{CW}} = -72.7\text{ K}$ extracted from the fit is nearly twice higher than -42.6 K reported in K_2IrCl_6 [14], and suggests that temperatures

well above 170 K may be required for an accurate Curie-Weiss fitting.

The Θ_{CW} value gauges the strength of magnetic interactions. Its increase in the bromide compared to the chloride has been cross-checked by high-field magnetization measurements. In the inset of Fig. 12, we show the magnetization measured up to 57 T in pulsed field and extrapolated to the expected saturation magnetization of $1 \mu_B/\text{f.u.}$ The resulting saturation field of 132 T is indeed much higher than 87 T estimated for K_2IrCl_6 [14]. We conclude that the substitution of Cl by Br increases magnetic interactions by 50 – 70%.

The $\chi(T)$ maximum around 14 K indicates the onset of antiferromagnetic order. The exact Néel temperature $T_N = 11.7 \text{ K}$ was determined from the peak in Fisher's heat capacity $d(\chi T)/dT$ in agreement with the specific heat data (Fig. 13). Below T_N , the susceptibility remains nearly isotropic, with no significant difference observed when the field is applied along $\langle 100 \rangle_c$, $\langle 110 \rangle_c$, and $\langle 111 \rangle_c$ [30]. This seeming absence of magnetic anisotropy even in the long-range ordered state may be related to the formation of magnetic domains and/or to the possible twinning of the crystal upon the structural phase transitions.

B. Specific heat

Temperature-dependent specific heat tracks the $\alpha - \beta$ transition around 170 K and the magnetic ordering transition at 11.9 K. Symmetric shape of the former peak is consistent with the first-order character of the structural phase transition. On the other hand, the peak at 12 K is reminiscent of a λ -type anomaly and suggests second-order nature of the transition, which is confirmed by the absence of hysteresis in thermal expansion [48]. We thus expect that no significant structural changes occur in K_2IrBr_6 upon magnetic ordering. Applied magnetic field shifts the transition toward lower temperatures (inset of Fig. 13a).

Lattice contribution was estimated by measuring specific heat of non-magnetic K_2PtBr_6 . Magnetic specific heat C_{mag} of K_2IrBr_6 obtained by subtraction was used to estimate magnetic entropy as

$$S_{\text{mag}}(T) = \int_0^T \frac{C_{\text{mag}}}{T'} dT'. \quad (5)$$

The resulting magnetic entropy is shown in the inset of Fig. 13b and reaches only 63% of $R \ln 2$ expected for $j_{\text{eff}} = \frac{1}{2}$ moments. We posit that K_2PtBr_6 may not be the best reference compound for K_2IrBr_6 , because even isostructural compounds of adjacent chemical elements sometimes show non-matching phonon spectra and, therefore, different lattice contributions to the specific heat [39]. The presence of soft phonon modes and structural phase transitions exacerbates this situation. Indeed, the Curie-Weiss temperature of -72.7 K suggests that a fraction of magnetic entropy should be released

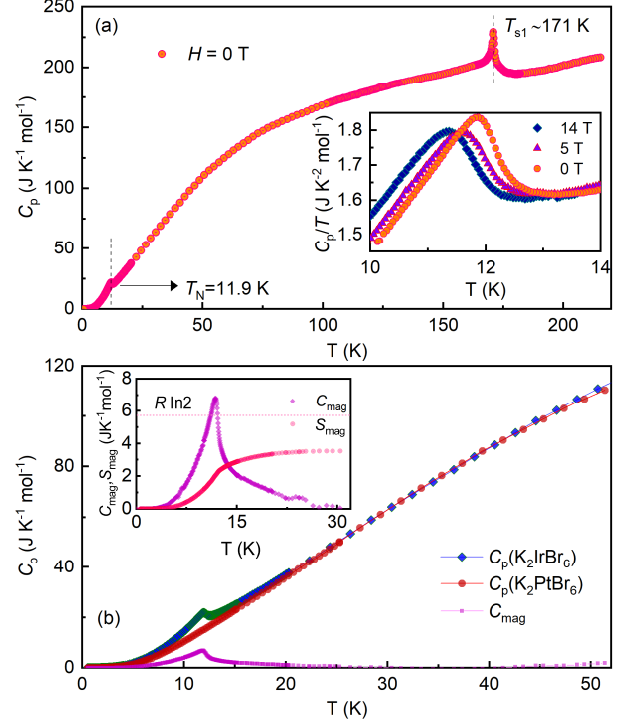


FIG. 13. (a) Temperature dependence of zero-field specific heat (C_p) measured on a single crystal from 220 K down to 0.5 K exhibits two anomalies at T_{s1} and T_N . The inset shows C_p/T as a function of T for $\mu_0 H = 0, 5$, and 14 with $H \parallel \langle 111 \rangle_c$. (b) Temperature dependence of the specific heat C_p of the non-magnetic K_2PtBr_6 , used as the reference data to subtract the lattice contribution. The evaluated magnetic contribution C_{mag} and the estimated magnetic entropy S_{mag} are shown in the inset for zero field. The dotted line refers to the magnetic entropy of $S_{\text{mag}} = R \ln(2j + 1)$ for $j = \frac{1}{2}$.

above 30 K, but this can't be seen when K_2PtBr_6 data are used as the reference.

We nevertheless expect that our lattice contribution should be rather accurate at low temperatures. Only 50% of total magnetic entropy is released below T_N , indicating that magnetic frustration is not insignificant, similar to some of the Ir^{4+} double perovskites that also feature a distorted version of the frustrated fcc spin lattice [49].

C. Microscopic magnetic model

Exchange couplings in Ir^{4+} compounds are described by the spin Hamiltonian

$$\mathcal{H} = \sum_{\langle ij \rangle} \mathbf{S}_i \mathbb{J}_{ij} \mathbf{S}_j, \quad (6)$$

TABLE II. The Ir–Ir distances (in Å) and main components of the exchange tensors (in K) calculated for the 20 K structure of γ -K₂IrBr₆. $|\mathbf{D}|$ is the length of the Dzyaloshinskii-Moriya vector. For the notation of individual interactions see Fig. 14.

| | $d_{\text{Ir-Ir}}$ | J | K | Γ | $ \mathbf{D} $ |
|----------------|--------------------|------|-----|----------|----------------|
| \mathbb{J}_1 | 7.132 | 20.0 | 8.9 | 1.5 | 0 |
| \mathbb{J}_2 | 7.131 | 15.8 | 7.4 | -0.9 | 0 |
| \mathbb{J}_3 | 7.132 | 20.0 | 8.9 | 1.5 | 0 |
| \mathbb{J}_4 | 7.131 | 15.8 | 7.4 | -0.9 | 0 |
| \mathbb{J}_5 | 7.243 | 15.7 | 5.7 | 2.1 | 12.1 |
| \mathbb{J}_6 | 7.269 | 14.0 | 4.6 | -3.0 | 13.3 |
| \mathbb{J}_7 | 7.269 | 14.0 | 4.6 | 3.0 | 13.8 |
| \mathbb{J}_8 | 7.243 | 15.7 | 5.7 | -2.1 | 12.1 |

with $S = \frac{1}{2}$ and the sum taken over atomic pairs. The \mathbb{J}_{ij} 's are exchange tensors of the form:

$$\mathbb{J}_{ij} = \begin{pmatrix} J + \Gamma_{xx} & D_z + \Gamma_{xy} & -D_y + \Gamma_{xz} \\ -D_z + \Gamma_{xy} & J + \Gamma_{yy} & D_x + \Gamma_{yz} \\ D_y + \Gamma_{xz} & -D_x + \Gamma_{yz} & J + \Gamma_{zz} \end{pmatrix},$$

where J is the isotropic (Heisenberg) coupling, $\mathbf{D} = (D_x, D_y, D_z)$ is the Dzyaloshinskii-Moriya (DM) interaction vector, and Γ describes the symmetric portion of anisotropic exchange.

In the cubic structure of K₂IrCl₆, each exchange tensor is reduced to the simpler form

$$\mathbb{J}_{xy} = \begin{pmatrix} J & \pm\Gamma & 0 \\ \pm\Gamma & J & 0 \\ 0 & 0 & J + K \end{pmatrix} \quad (7)$$

where diagonal part of the anisotropic exchange is reduced to the isotropic Kitaev term K , off-diagonal part is restricted to the single component Γ , and DM interactions are forbidden by symmetry. The exchange parameters $J \simeq 13$ K, $K \simeq 5$ K, and $\Gamma \simeq 1$ K were determined from superexchange theory of Refs. 50 and 51 using the optimal value of $U = 2.2$ eV.

Full exchange tensors determined for the 20 K crystal structure of γ -K₂IrBr₆ using the same method and $U = 1.8$ eV are given in the Supplemental Material [30]. In both cases, hopping parameters were obtained by Wannier projections that take covalency effects into account. Lower symmetry of K₂IrBr₆ causes exchange tensors to deviate from the simple form of Eq. (7), although one can still recognize a similar structure and introduce effective values of J as the isotropic coupling, K as the leading diagonal anisotropy, and Γ as the leading symmetric off-diagonal anisotropy, augmented by Dzyaloshinskii-Moriya vectors \mathbf{D} for bonds $\mathbb{J}_5 - \mathbb{J}_8$ without inversion symmetry.

The monoclinic structure of γ -K₂IrBr₆ features 8 nonequivalent nearest-neighbor exchange pathways

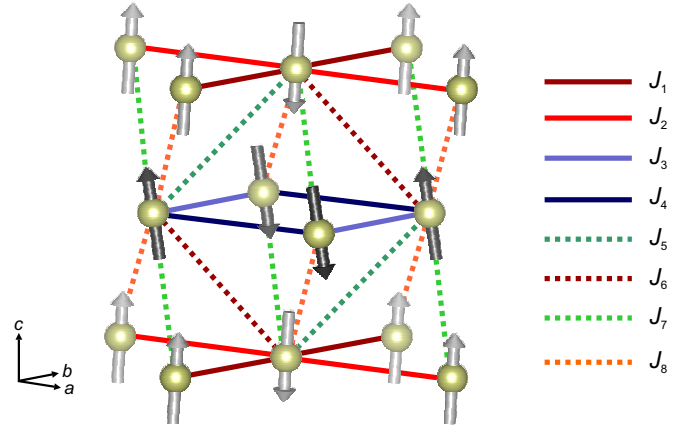


FIG. 14. Distorted fcc spin lattice in the γ -phase of K₂IrBr₆. Crystallographic directions of the monoclinic γ -structure are shown. The spin configuration of canted type-I order, as obtained from DFT+ U +SO calculations, is superimposed (see text for details).

shown in Fig. 14. The corresponding interactions are listed in Table II. In contrast to the regular fcc lattice, each triangular loop includes three couplings of different strength. This partially alleviates the frustration and explains the change in the frustration ratio Θ_{CW}/T_N from 13.7 in K₂IrCl₆ [14] to 6.0 in K₂IrBr₆.

We also find up to 50% increase in the magnitude of exchange couplings compared to K₂IrCl₆. This increase should be traced back to the reduced strength of electronic correlations and, eventually, to the enhanced covalency of the Ir–Br interactions (see Sec. IV B). The hierarchy of hopping parameters does not change significantly. Therefore, all interactions $\mathbb{J}_1 - \mathbb{J}_8$ feature large Heisenberg exchange with a weaker antiferromagnetic Kitaev exchange and minor off-diagonal anisotropy.

The fcc antiferromagnets with predominant nearest-neighbor couplings feature two types of collinear magnetic order known as type-I and type-III [52]. We computed energies of type-I and type-III spin configurations of γ -K₂IrBr₆ in DFT+ U +SO (in VASP) while allowing magnetic moment directions to relax. This led to the 1.6 meV/f.u. lower energy of the type-I order (Fig. 14), in agreement with the neutron results that revealed the propagation vector $\mathbf{k} = (\frac{1}{2}, \frac{1}{2}, 0)$ compatible with the type-I order. Stabilization of this order is accompanied by a spin canting wherein four sublattices feature spins directed along $\pm(-0.075, -0.050, 0.996)$ and $\pm(0.254, -0.085, 0.963)$ within the Cartesian coordinate frame of γ -K₂IrBr₆. The sizable canting angle of 13.7° is probably a result of large DM couplings on some of the bonds.

VI. DISCUSSION AND SUMMARY

The non-cubic crystal-field splitting of $\Delta = 50 - 70$ meV observed in K₂IrBr₆ and other Ir⁴⁺ antiferro-

rites [16] is remarkably smaller than in Ir^{4+} oxides with weakly distorted IrO_6 octahedra. Larger deformations of the octahedra enhance Δ significantly. For example, post-perovskite CaIrO_3 reveals $\Delta = -0.71$ eV [42] for the tetragonal distortion of $\delta_t = -1.9\%$. Our calculations (Fig. 10) suggest that a similar distortion in the bromide would lead to only a small $\Delta \simeq 0.01$ eV.

This much weaker crystal-field splitting can be traced back to the reduced charge of the ligand and the enhanced covalency that both weaken electrostatic effects on the Ir $5d$ orbitals. The crystal-field splitting as low as 50 meV can be reached in this way. Its size appears to be determined not only by deformations of the IrBr_6 octahedron, but also by the positions of more distant neighbors such as K^+ ions. On one hand, this creates a large flexibility. Different types of distortions compensate each other and keep Δ small, as in the γ -phase of K_2IrBr_6 . On the other hand, residual crystal-field splittings are hard to eliminate in this setting, because virtually every structural distortion, be it static in monoclinic γ - K_2IrBr_6 or dynamic in cubic α - K_2IrBr_6 , renders Δ non-zero. Reaching $\Delta = 0$ and the pure, unperturbed $j_{\text{eff}} = \frac{1}{2}$ state appears to be exceedingly difficult, because even effects like zero-point motions and vibronic couplings are likely to affect crystal-field levels of Ir^{4+} .

In summary, we reported and elucidated structural transformations in K_2IrBr_6 and their effect on the non-cubic crystal-field splitting Δ for the Ir^{4+} ion. Relevant structural distortions are separated into two groups. Tensile tetragonal strain and octahedral rotations on one side and octahedral tilts as well as orthorhombic deformations of the IrBr_6 octahedra on the other side lead to antagonistic changes in Δ . These changes underlie the non-monotonic evolution of Δ across the structural phase transitions. The transitions cause a distortion of the fcc spin lattice and partially alleviate magnetic frustration. Magnetic couplings are similar in nature to the cubic Ir^{4+} hexahalides, with the predominant Heisenberg term and

a weak antiferromagnetic Kitaev term, but show a larger magnitude thanks to the reduced correlations on the Ir site. This way, covalency not only reduces crystal-field splittings, but also enhances magnetic couplings. Type-I magnetic order is stabilized, albeit with a large spin canting caused by the underlying structural distortion.

ACKNOWLEDGMENTS

NK thanks Somnath Ghara for his help with resistivity measurements. AAT thanks Adam Aczel and Anna Efimenko for fruitful discussions on the Ir^{4+} antiferrofluorites, and Yurii Skourski for performing the high-field magnetization measurements. The work in Augsburg was supported by the Federal Ministry for Education and Research through the Sofja Kovalevskaya Award of Alexander von Humboldt Foundation (AAT). The work was partially supported by the Ministry of Science and Higher Education of the Russian Federation (through the basic part of the government mandate, Project No. FEUZ-2020-0060).

We acknowledge ESRF and APS for providing synchrotron beamtime for this project, and thank Andy Fitch for his technical support during the experiment at ID22, ESRF. This research used resources of the Advanced Photon Source, a U.S. Department of Energy (DOE) Office of Science User Facility, operated for the DOE Office of Science by Argonne National Laboratory under Contract No. DE-AC02-06CH11357. Extraordinary facility operations were supported in part by the DOE Office of Science through the National Virtual Biotechnology Laboratory, a consortium of DOE national laboratories focused on the response to COVID-19, with funding provided by the Coronavirus CARES Act. We also acknowledge the support of the HLD at HZDR, member of European Magnetic Field Laboratory (EMFL).

-
- [1] W. Witczak-Krempa, G. Chen, Y. B. Kim, and L. Balents, Correlated quantum phenomena in the strong spin-orbit regime, *Ann. Rev. Condens. Matter Phys.* **5**, 57 (2014).
 - [2] J. G. Rau, E. K.-H. Lee, and H.-Y. Kee, Spin-orbit physics giving rise to novel phases in correlated systems: Iridates and related materials, *Ann. Rev. Condens. Matter Phys.* **7**, 195 (2016).
 - [3] S. Kanungo, B. Yan, P. Merz, C. Felser, and M. Jansen, Na_4IrO_4 : square-planar coordination of a transition metal in d^5 configuration due to weak on-site Coulomb interactions, *Angew. Chem. Int. Ed.* **54**, 5417 (2015).
 - [4] X. Ming, C. Autieri, K. Yamauchi, and S. Picozzi, Role of square planar coordination in the magnetic properties of Na_4IrO_4 , *Phys. Rev. B* **96**, 205158 (2017).
 - [5] S. M. Winter, A. A. Tsirlin, M. Daghofer, J. van den Brink, Y. Singh, P. Gegenwart, and R. Valentí, Models and materials for generalized Kitaev magnetism, *J. Phys.: Condens. Matter* **29**, 493002 (2017).
 - [6] G. Cao and P. Schlottmann, The challenge of spin-orbit-tuned ground states in iridates: a key issues review, *Rep. Prog. Phys.* **81**, 042502 (2018).
 - [7] J. Bertinshaw, Y. K. Kim, G. Khaliullin, and B. J. Kim, Square lattice iridates, *Ann. Rev. Condens. Matter Phys.* **10**, 315 (2019).
 - [8] H. Gretarsson, J. P. Clancy, X. Liu, J. P. Hill, E. Bozin, Y. Singh, S. Manni, P. Gegenwart, J. Kim, A. H. Said, D. Casa, T. Gog, M. H. Upton, H.-S. Kim, J. Yu, V. M. Katukuri, L. Hozoi, J. van den Brink, and Y.-J. Kim, Crystal-field splitting and correlation effect on the electronic structure of A_2IrO_3 , *Phys. Rev. Lett.* **110**, 076402 (2013).
 - [9] A. A. Aczel, J. P. Clancy, Q. Chen, H. D. Zhou, D. Reig-i-Plessis, G. J. MacDougall, J. P. C. Ruff, M. H. Upton, Z. Islam, T. J. Williams, S. Calder, and J.-Q. Yan, Revisiting the Kitaev material candidacy of Ir^{4+} double

- perovskite iridates, *Phys. Rev. B* **99**, 134417 (2019).
- [10] A. Revelli, C. C. Loo, D. Kiese, P. Becker, T. Fröhlich, T. Lorenz, M. Moretti Sala, G. Monaco, F. L. Buessen, J. Attig, M. Hermanns, S. V. Streltsov, D. I. Khomskii, J. van den Brink, M. Braden, P. H. M. van Loosdrecht, S. Trebst, A. Paramekanti, and M. Grüninger, Spin-orbit entangled $j = \frac{1}{2}$ moments in $\text{Ba}_2\text{CeIrO}_6$: A frustrated fcc quantum magnet, *Phys. Rev. B* **100**, 085139 (2019).
 - [11] M. Rossi, M. Retegan, C. Giacobbe, R. Fumagalli, A. Efimenko, T. Kulka, K. Wohlfeld, A. I. Gubanov, and M. Moretti Sala, Possibility to realize spin-orbit-induced correlated physics in iridium fluorides, *Phys. Rev. B* **95**, 235161 (2017).
 - [12] Note that Ref. [9] refers to Δ as the splitting between the RIXS peaks, Δ_{exp} . In contrast, our Δ is the actual splitting between the t_{2g} levels, and $\Delta = \frac{3}{2}\Delta_{\text{exp}}$ in the limit of $\Delta \ll \lambda$, where $\lambda \simeq 0.4 - 0.5 \text{ eV}$ is the typical spin-orbit coupling in Ir^{4+} compounds.
 - [13] M. E. Lines, Antiferromagnetism in the face-centred cubic lattice by a spin-wave method, *Proc. Royal Soc. A* **271**, 105 (1963).
 - [14] N. Khan, D. Prishchenko, Y. Skourski, V. G. Mazurenko, and A. A. Tsirlin, Cubic symmetry and magnetic frustration on the fcc spin lattice in K_2IrCl_6 , *Phys. Rev. B* **99**, 144425 (2019).
 - [15] R. Schick, T. Ziman, and M. E. Zhitomirsky, Quantum versus thermal fluctuations in the fcc antiferromagnet: Alternative routes to order by disorder, *Phys. Rev. B* **102**, 220405(R) (2020).
 - [16] D. Reig-i Plessis, T. A. Johnson, K. Lu, Q. Chen, J. P. C. Ruff, M. H. Upton, T. J. Williams, S. Calder, H. D. Zhou, J. P. Clancy, A. A. Aczel, and G. J. MacDougall, Structural, electronic, and magnetic properties of nearly ideal $J_{\text{eff}} = \frac{1}{2}$ iridium halides, *Phys. Rev. Materials* **4**, 124407 (2020).
 - [17] V. Petříček, M. Dušek, and L. Palatinus, Crystallographic computing system JANA2006: General features, *Z. Krist.* **229**, 345 (2014).
 - [18] R. Küchler, A. Wörl, P. Gegenwart, M. Berben, B. Bryant, and S. Wiedmann, The world's smallest capacitive dilatometer, for high-resolution thermal expansion and magnetostriction in high magnetic fields, *Rev. Sci. Instr.* **88**, 083903 (2017).
 - [19] A. A. Tsirlin, B. Schmidt, Y. Skourski, R. Nath, C. Geibel, and H. Rosner, Exploring the spin- $\frac{1}{2}$ frustrated square lattice model with high-field magnetization studies, *Phys. Rev. B* **80**, 132407 (2009).
 - [20] K. Koepernik and H. Eschrig, Full-potential nonorthogonal local-orbital minimum-basis band-structure scheme, *Phys. Rev. B* **59**, 1743 (1999).
 - [21] A. Togo and I. Tanaka, First principles phonon calculations in materials science, *Scr. Mater.* **108**, 1 (2015).
 - [22] G. Kresse and J. Furthmüller, Efficiency of *ab-initio* total energy calculations for metals and semiconductors using a plane-wave basis set, *Computational Materials Science* **6**, 15 (1996).
 - [23] G. Kresse and J. Furthmüller, Efficient iterative schemes for *ab initio* total-energy calculations using a plane-wave basis set, *Phys. Rev. B* **54**, 11169 (1996).
 - [24] J. P. Perdew, K. Burke, and M. Ernzerhof, Generalized gradient approximation made simple, *Phys. Rev. Lett.* **77**, 3865 (1996).
 - [25] K. Rössler and J. Winter, Influence of *d*-electron configuration on phase transitions in A_2MX_6 (Hexahalometalates IV), *Chem. Phys. Lett.* **46**, 566 (1977).
 - [26] A. I. Gubanov, S. A. Gromilov, S. V. Korenev, A. B. Venediktov, and I. P. Asanov, Synthesis and study of potassium hexabromoiridate(IV), *Russ. J. Coord. Chem.* **28**, 864 (2002).
 - [27] W. Abriel, Crystal structure and phase transition of Rb_2TeI_6 , *Mater. Res. Bull.* **17**, 1341 (1982).
 - [28] W. Abriel, Polymorphism and phase transitions of K_2TeBr_6 : A single crystal investigation of the high temperature phases (383–463 K), *Mater. Res. Bull.* **19**, 313 (1984).
 - [29] S. C. Abrahams, J. Ihringer, P. Marsh, and K. Nassau, Phase transition at 434 K, independent strain coupling in second transition at 400 K, and thermal expansivity in ferroelastic K_2TeBr_6 , *J. Chem. Phys.* **81**, 2082 (1984).
 - [30] See Supplemental Material for additional XRD data and structure refinements, as well as additional magnetization data, exchange tensors, and details of DFT calculations.
 - [31] J. W. Lynn, H. H. Patterson, G. Shirane, and R. G. Wheeler, Soft rotary mode and structural phase transitions in K_2ReCl_6 , *Solid State Comm.* **27**, 859 (1978).
 - [32] D. Mintz, R. L. Armstrong, B. M. Powell, and W. J. L. Buyers, Soft rotary mode in the antiferrocrystal K_2OsCl_6 , *Phys. Rev. B* **19**, 448 (1979).
 - [33] M. Sutton, R. L. Armstrong, B. M. Powell, and W. J. L. Buyers, Lattice dynamics and phase transitions in antiferrocrystals: K_2OsCl_6 , *Phys. Rev. B* **27**, 380 (1983).
 - [34] V. Novotny, C. A. Martin, R. L. Armstrong, and P. P. M. Meincke, Thermodynamical properties of K_2OsCl_6 and K_2ReCl_6 at low temperatures and near their structural phase transitions, *Phys. Rev. B* **15**, 382 (1977).
 - [35] R. L. Armstrong, D. Mintz, B. M. Powell, and W. J. L. Buyers, Ferrorotative transition in the antiferrocrystal K_2OsCl_6 , *Phys. Rev. B* **17**, 1260 (1978).
 - [36] H. W. Willemsen, C. A. Martin, P. P. M. Meincke, and R. L. Armstrong, Thermal-expansion study of the displacive phase transitions in K_2ReCl_6 and K_2OsCl_6 , *Phys. Rev. B* **16**, 2283 (1977).
 - [37] R. A. Cowley, Structural phase transitions I. Landau theory, *Adv. Phys.* **29**, 1 (1980).
 - [38] H. M. Van Driel, M. Wiszniewska, B. M. Moores, and R. L. Armstrong, Softening of the rotary lattice mode in K_2PtBr_6 as detected by nuclear quadrupole resonance, *Phys. Rev. B* **6**, 1596 (1972).
 - [39] S. Widmann, V. Tsurkan, D. A. Prishchenko, V. G. Mazurenko, A. A. Tsirlin, and A. Loidl, Thermodynamic evidence of fractionalized excitations in $\alpha\text{-RuCl}_3$, *Phys. Rev. B* **99**, 094415 (2019).
 - [40] Q. Huang, J. L. Soubeyroux, O. Chmaissem, I. Natali Sora, A. Santoro, R. J. Cava, J. J. Krajewski, and W. F. Peck Jr., Neutron powder diffraction study of the crystal structures of Sr_2RuO_4 and Sr_2IrO_4 at room temperature and at 10 K, *J. Solid State Chem.* **112**, 355 (1994).
 - [41] A. Nakatsuka, K. Sugiyama, A. Yoneda, K. Fujiwara, and A. Yoshiasa, Crystal structure of post-perovskite-type CaIrO_3 reinvestigated: new insights into atomic thermal vibration behaviors, *Acta Cryst.* **E71**, 1109 (2015).
 - [42] M. Moretti Sala, K. Ohgushi, A. Al-Zein, Y. Hirata, G. Monaco, and M. Krisch, CaIrO_3 : A spin-orbit Mott insulator beyond the $J_{\text{eff}} = \frac{1}{2}$ ground state, *Phys. Rev. Lett.* **112**, 176402 (2014).
 - [43] Here, we neglect the weak splitting of 3 – 4 meV that appears between the doubly-degenerate levels upon or-

thorhombic deformation.

- [44] N. A. Bogdanov, V. M. Katukuri, J. Romhányi, V. Yushankhai, V. Kataev, B. Büchner, J. van den Brink, and L. Hozoi, Orbital reconstruction in nonpolar tetravalent transition-metal oxide layers, [Nature Comm. **6**, 7306 \(2015\)](#).
- [45] J. W. Lynn, G. Shirane, and M. Blume, Covalency effects in the magnetic form factor of Ir in K_2IrCl_6 , [Phys. Rev. Lett. **37**, 154 \(1976\)](#).
- [46] G. A. Bain and J. F. Berry, Diamagnetic corrections and Pascal's constants, [J. Chem. Education **85**, 532 \(2008\)](#).
- [47] M. Majumder, F. Freund, T. Dey, M. Prinz-Zwick, N. Büttgen, Y. Skourski, A. Jesche, A. A. Tsirlin, and P. Gegenwart, Anisotropic temperature-field phase diagram of single crystalline $\beta\text{-Li}_2\text{IrO}_3$: Magnetization, specific heat, and ^7Li NMR study, [Phys. Rev. Materials **3**, 074408 \(2019\)](#).
- [48] Specific heat does not show thermal hysteresis at any of the transitions because of long heat pulses used in the relaxation method.
- [49] G. Cao, A. Subedi, S. Calder, J.-Q. Yan, J. Yi, Z. Gai, L. Poudel, D. J. Singh, M. D. Lumsden, A. D. Christianson, B. C. Sales, and D. Mandrus, Magnetism and electronic structure of $\text{La}_2\text{ZnIrO}_6$ and $\text{La}_2\text{MgIrO}_6$: Candidate $J_{\text{eff}} = \frac{1}{2}$ Mott insulators, [Phys. Rev. B **87**, 155136 \(2013\)](#).
- [50] J. G. Rau, E. K.-H. Lee, and H.-Y. Kee, Generic spin model for the honeycomb iridates beyond the Kitaev limit, [Phys. Rev. Lett. **112**, 077204 \(2014\)](#).
- [51] S. M. Winter, Y. Li, H. O. Jeschke, and R. Valentí, Challenges in design of Kitaev materials: Magnetic interactions from competing energy scales, [Phys. Rev. B **93**, 214431 \(2016\)](#).
- [52] D. Ter Haar and M. Lines, A spin-wave theory of anisotropic antiferromagnetica, [Phil. Trans. Royal Soc. A **255**, 1 \(1962\)](#).

Supplemental Material

Toward cubic symmetry for Ir^{4+} : structure and magnetism of the antifluorite K_2IrBr_6

A. Crystal structure

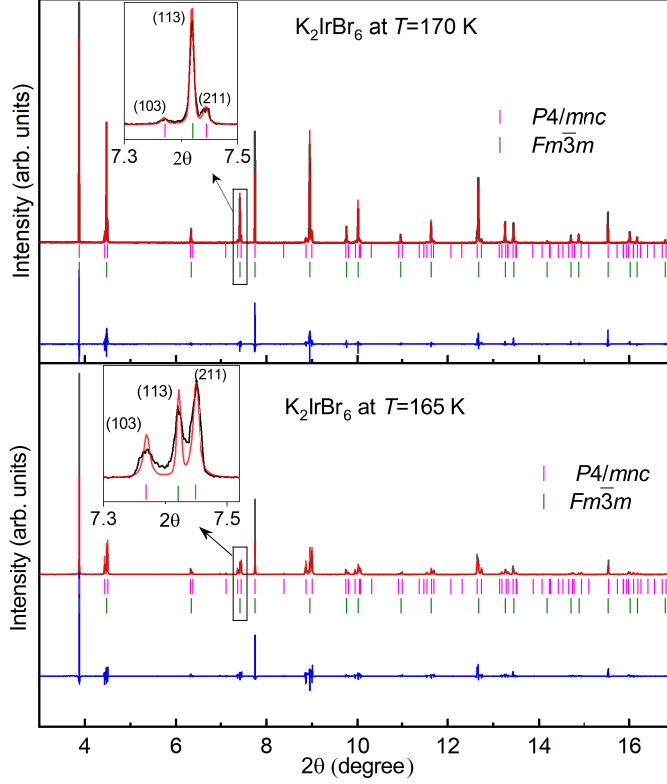


FIG. S1. Refined synchrotron powder X-ray diffraction patterns of K_2IrBr_6 in the temperature range of phase coexistence upon the $\alpha - \beta$ transition.

In Fig. S1, we show structure refinements in the vicinity of the $\alpha - \beta$ transition to highlight phase coexistence at 165 and 170 K.

Refinement residuals R_I and R_p use standard definitions of JANA2006. The intensity-based R -value is determined via integrated reflection intensities I_i ,

$$R_I = \frac{\sum_i |I_i^{\text{obs}} - I_i^{\text{calc}}|}{\sum_i I_i^{\text{obs}}}. \quad (\text{S1})$$

In contrast, the profile-based R_p gauges the agreement at each point of the powder profile,

$$R_p = \frac{\sum_i |y_i^{\text{obs}} - y_i^{\text{calc}}|}{\sum_i y_i^{\text{obs}}}, \quad (\text{S2})$$

where y_i is the observed (calculated) intensity at a given 2θ angle.

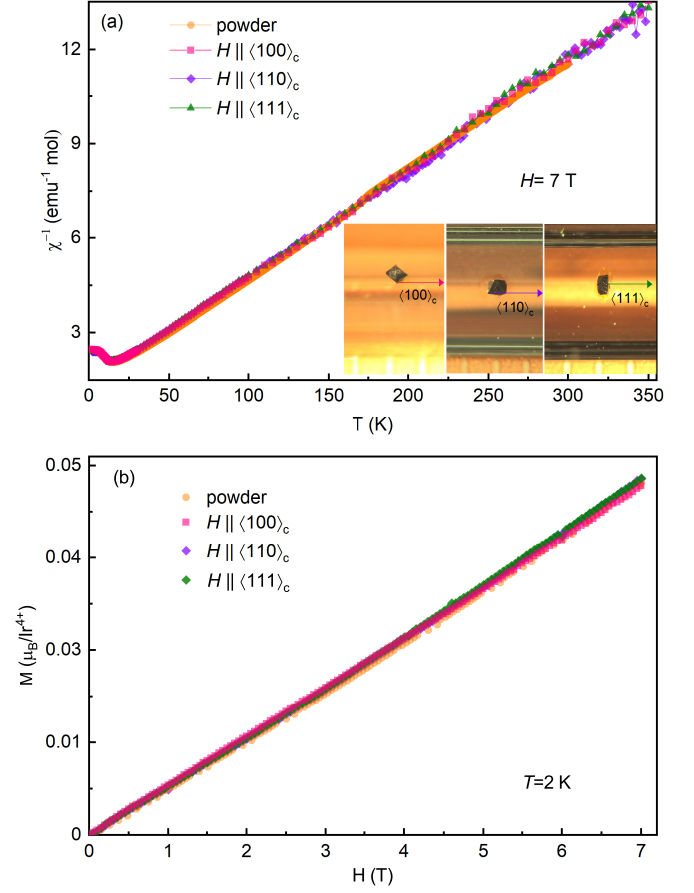


FIG. S2. Temperature dependence of the inverse susceptibility (a), and field dependence of the magnetization at 2 K (b) measured on a 0.29 mg K_2IrBr_6 single crystal in the field $\mu_0 H = 7$ T applied along $\langle 100 \rangle_c$, $\langle 110 \rangle_c$, and $\langle 111 \rangle_c$ directions. The data for powder sample are superimposed.

B. Magnetic susceptibility

In Fig. S2, we show field- and temperature-dependent magnetization measurements on an individual single crystal of K_2IrBr_6 . The data are somewhat noisy because of the very small crystal mass, but clearly show the absence of magnetic anisotropy, in agreement with the $j_{\text{eff}} = \frac{1}{2}$ state of Ir^{4+} .

C. Crystal-field splitting

The effect of individual structural distortions on the crystal-field splitting Δ was studied for several model structures. They were constructed as follows:

- Octahedral rotations (φ): space group $P4/mnc$, the octahedra are kept rigid and rotate in the ab plane
- Octahedral tilts (ψ): space group $I2/m$, the octahedra are kept rigid and tilt in the ab plane
- Tetragonal strain (η): space group $P4/mnc$, the Br positions are adjusted in such a way that the Ir–Br distances remain constant
- Tetragonal deformation (δ_t): space group $P4/mnc$, the Br positions are adjusted in such a way that the average Ir–Br distance $(d_1 + d_2)/2$ remains constant
- Orthorhombic deformation (δ_o): space group $Fmmm$, the Br positions are adjusted in such a way that $(d_1 + d'_1)/2 = d_2$ remains constant

In all cases except δ_o , the tetragonal/monoclinic unit cell of β -/ γ - K_2IrBr_6 was used. In the case of δ_o , the unit cell of α - K_2IrBr_6 was used but with the lower symmetry to allow for the deformation. Scalar-relativistic calculations were performed, and orbital energies of the t_{2g} manifold were obtained by Wannier projections.

D. Exchange couplings

Exchange couplings were estimated for the 20 K structure of γ - K_2IrBr_6 using superexchange theory of Refs. [50] and [51] with the effective Coulomb repulsion $U = 1.8$ eV, Hund's coupling $J = 0.3$ eV, and spin-orbit coupling constant $\lambda = 0.4$ eV. Individual exchange tensors are given below. All components are in units of Kelvin. For the notation of bonds, see main text.

$$\mathbb{J}_1 = \begin{pmatrix} 20.1 & 1.5 & -0.3 \\ 1.5 & 20.0 & 0.5 \\ -0.3 & 0.5 & 28.9 \end{pmatrix}$$

$$\mathbb{J}_2 = \begin{pmatrix} 15.8 & -0.9 & 0.6 \\ -0.9 & 15.7 & 0 \\ 0.6 & 0 & 23.2 \end{pmatrix}$$

$$\mathbb{J}_3 = \begin{pmatrix} 20.0 & 1.5 & -0.5 \\ 1.5 & 20.1 & 0.3 \\ -0.5 & 0.3 & 28.9 \end{pmatrix}$$

$$\mathbb{J}_4 = \begin{pmatrix} 15.7 & -0.9 & 0 \\ -0.9 & 15.8 & -0.6 \\ 0 & -0.6 & 23.2 \end{pmatrix}$$

$$\mathbb{J}_5 = \begin{pmatrix} 14.9 & 10.4 & 5.4 \\ -10.3 & 21.3 & 4.6 \\ -1.1 & -6.2 & 16.4 \end{pmatrix}$$

$$\mathbb{J}_6 = \begin{pmatrix} 14.4 & 8.9 & -2.1 \\ -8.3 & 18.6 & -10.3 \\ -4.0 & 9.3 & 13.6 \end{pmatrix}$$

$$\mathbb{J}_7 = \begin{pmatrix} 18.6 & 9.0 & -10.0 \\ -8.3 & 14.4 & 5.3 \\ 10.9 & 0.8 & 13.6 \end{pmatrix}$$

$$\mathbb{J}_8 = \begin{pmatrix} 21.3 & 10.4 & 6.4 \\ -10.3 & 14.9 & 0.8 \\ -4.7 & -5.1 & 16.4 \end{pmatrix}$$

Note that $\mathbb{J}_1 - \mathbb{J}_4$ are symmetric, because inversion centers in the middle of the bonds render $\mathbf{D} = 0$. In contrast, $\mathbb{J}_5 - \mathbb{J}_8$ lack such inversion symmetry and entail sizable Dzyaloshinskii-Moriya interactions.